Full Paper

Hot Spot Chemistry in Several Polymer-Bound Explosives under Nanosecond Shock Conditions

Will P. Bassett,*[a] Belinda P. Johnson,[b] and Dana D. Dlott[b]

Abstract: Initial hot spot temperatures and temperature evolutions for 4 polymer-bound explosives under shock compression by laser-driven flyer plates at speeds from 1.5–4.5 km s^{-1} are presented. A new averaging routine allows for improved signal to noise in shock compressed impactor experiments and yields temperature dynamics which are more accurate than has been previously available. The PBX formulations studied here consist of either pentaerythritol tetranitrate (PETN), 1,3,5-trinitro-1,3,5-triazinane (RDX), 2,4,6-trinitrotoluene (TNT), or 1,3,5-triamino-2,4,6-trinitrobenzene (TATB) in a 80/20 wt.% mixture with a silicone elastomer binder. The temperature dynamics demonstrate a unique shock strength dependence for each base explosive. The initial hot spot temperature and its evolution in time are shown to be indicative of chemistry occurring within the reaction zone of the four explosives. The number density of hot spots is qualitatively inferred from the spatially-averaged emissivity and appears to increase exponentially with shock strength. An increased emissivity for formulations consisting of TNT and TATB is consistent with carbon-rich explosives and in increased hot spot volume. Qualitative conclusions about sensitivity were drawn from the initial hot spot temperature and rate at which the number of hot spots appear to grow.

Keywords: PBX · Pyrometry · Emission Spectra · PETN · RDX · TNT · TATB

1 Introduction

Shock initiation of energetic materials (EMs) is a complex mechanochemical phenomenon which is inherently difficult to experimentally probe due to the vast time and space scales over which reaction occur [1]. This is especially true for polymer-bound explosives (PBXs), where a relatively high degree of heterogeneity is present as crystal/crystal, crystal/binder, and crystal/void interfaces. In the present work, we have made significant progress in characterizing the temperatures of the initial localized reaction zones, known as hot spots, and the subsequent reactivity which hot spots undergo as it relates to the fundamentals of the EM-base from which the PBX is created. The EMs studied in this work are pentaerythritol tetranitrate (PETN), 1,3,5-trinitro-1,3,5-triazinane (RDX), 2,4,6-trinitrotoluene (TNT), and 1,3,5-triamino-2,4,6-trinitrobenzene (TATB) and consist of 80 wt.% EM and 20 wt.% elastomer binder, similar to known materials XTX-8003 and XTX-8004 which have a PETN and RDX base, respectively [2,3].

In polymer-bound systems without micron-scale void features, we've shown that hot spots originate from shock-induced decomposition of the reactive material and subsequent compression into what is best described as a reactive fluid (i.e. a hot, dense amalgam of EM and EM decomposition products such as H_2O, N_2, CO, etc.) [4,5]. The fundamental processes which form these reactive fluids as they decompose from the starting material and give rise to hot spots occurs on the ps timescale and thus are too quick to be observed by our pyrometer [6–8]. The initial temper-ature and temperature evolution of these reactive hot spots, as dictated by the starting material and thus chemical environment, as a function of relative shock strength is the subject of this publication. Pyrometry is particularly suited to hot spot temperature studies due to the well-known bias towards observing the highest temperatures rather than the bulk or average temperature [9].

Purely physics based simulations of hot spot formation rarely show hot spot temperatures which are sufficient to initiate reaction [10,11]. Recently, simulations of PETN and RDX which include chemical reaction have observed hot spot temperatures on the order of ~4000 K for collapsing pores which are 10–100 nm in diameter [6,7]. These temperatures are consistent with those our group observed recently in PBX systems based on PETN [4]. As reported previously, the hot spot temperatures were observed concurrent with impact without a measurable temperature rise time, indicating the local temperatures under shock compression reached 4000 K in < 4 ns, which corresponds to a heating rate of > 10^{12} K/s. The capability to measure

[a] W. P. Bassett
Energetic Materials Center
Lawrence Livermore National Laboratory
7000 East Ave, Livermore, CA 94550 USA
*e-mail: bassett3@llnl.gov

[b] B. P. Johnson, D. D. Dlott
School of Chemical Sciences and Fredrick Seitz Materials Research Laboratory
University of Illinois at Urbana-Champaign, Urbana, Il 61801 USA

temperature evolutions during initiation of EMs is instrumental in informing models and increasing our basic understanding of the physical and chemical processes of shock initiation [12]. A fundamental understanding of these processes will help efforts to improve the heavily parameterized phenomenological models for EM ignition which have been utilized for modeling EM initiation thresholds and reaction processes in bulk systems for the last 30 years [13].

The high explosive components in the formulations studied here were considered because of their well-known differences in reaction zone length, chemistry, and sensitivity. Reaction zone studies reported by Tarver suggest that the formulations studied here should behave on fundamentally different time scales [14]. PETN was chosen due to its small reaction zone ($<$ 10 ns) that causes it to behave consistent with pure CJ theory (i.e. no measureable reaction zone in pressed pellets) according to particle velocity data [15]. RDX was chosen due to its slower chemistry, where most of the energy is liberated over 20 ns, and relatively high oxygen balance which is lower than PETN, but much greater than TNT and TATB [14]. TNT and TATB were chosen due to their similar chemistry, with reaction zones lasting several hundred nanoseconds, where TNT trades enhanced power for enhanced sensitivity [14]. It is interesting to note that with the exception of PETN, the reaction zone is spatially long enough in each explosive that when the shock front passes through the length of our charges, ~40 μm, and reaches the substrate, reaction at the flyer/EM interface has nominally not reached chemical equilibrium and ceased reaction. In the rest of this publication, we describe the experimental apparatus and experiments which were conducted, present and discuss shock strength-dependent hot spot temperature evolutions for the 4 formulations, discuss the implications of the qualitatively measured hot spot number density, and analyze the mechanisms which control hot spot temperature evolution.

2 Experimental Section

Laser-driven thin Al foils (flyer plates) were launched in a vacuum by a shock-assisted method that does not significantly heat the flyers [16]. The experimental concept is depicted in Figure 1a. The plates impacted polymer-bound explosive (PBX) samples in wells 1 mm in diameter and 42 μm thick. A 10X Olympus microscope objective (10X-LMPLFLN) transmitted and received 1.55 μm light from a photon Doppler velocimeter (PDV) used to determine flyer plate velocities and collected the visible (442–850 nm) shock-induced emission [17].

The EM samples were placed in a shock target microarray, produced by placing a 42 μm thick Kapton tape with an array of 187 holes 1 mm diameter on a Starphire glass window (75×75×6.35 mm³). Samples were composed of 80 wt.% explosive (PETN, RDX, TNT, or TATB) and 20 wt.%
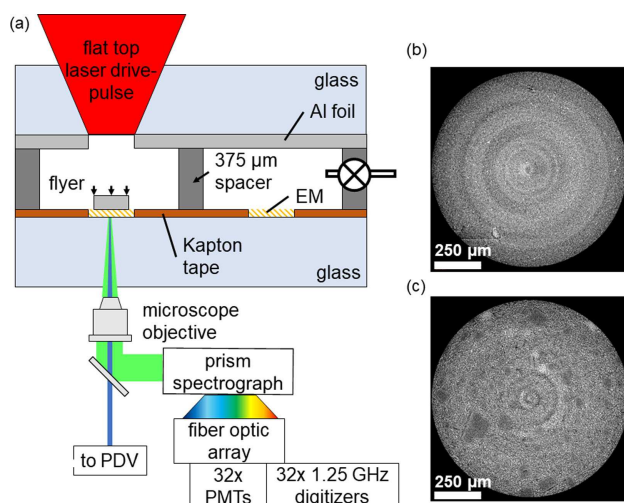
Figure 1. (a) Schematic of the experiment (not to scale). Tiny energetic material (EM) charges were fabricated in an array of 42 μm deep, 1 mm diameter wells. The glass substrate was 75×5×6.35 mm³. The Al foil was 25 μm thick. Representative 2D slices of 3D tomograms are shown for (b) X-RDX and (c) X-TNT.

poly(dimethylsiloxane) (PDMS, Sylgard 182), henceforth referred to as X-PETN, X-RDX, X-TNT, and X-TATB, respectively. The polymer was chosen to remove micron-scale void spaces [4] and approximate known PBXs XTX-8003 and XTX-8004 which are made using PETN and RDX, respectively [2,3]. No published results on an extrudable explosive (XTX) variant with a TATB or TNT base were available. Due to the lack of Hugoniot information available for X-TNT, and X-TATB, all shock states are reported simply as the flyer impactor velocity. A given velocity will likely not result in the same shock pressure across all materials, thus direct comparisons between materials for a given flyer velocity does not guarantee identical shock states. All PBX samples were made by the addition of fine grain HE to a solution of PDMS diluted in hexanes, stirred until the hexanes evaporated, and then transferred to a hydraulic press for homogenization. Infrared spectroscopy was used to confirm that no detectable quantities of residual solvents were present, indicating their concentration was at most $<$1%. Densities for the various HE materials was estimated by filling large (3 mm diameter×0.5 mm thick) wells. X-PETN and X-RDX were measured to have a density of corresponding to 99±3% of the theoretical maximum density (TMD), taken as the mass average of the component densities, whereas X-TNT and X-TATB exhibited lower densities, typically between 90–95% TMD. The uncertainty in TMD is likely due to variations in the exact binder/HE wt.%. Most HEs used here are ~2x as dense as PDMS, resulting in densities that may be higher than the nominal TMD if the true wt. % favors the explosive slightly. We have not quantified the wt. % uncertainty in our samples, but when formulated using extremely small quantities, as done here, it is likely to have some variation. Computer tomography (Xradia MicroXCT-

400) was performed on each PBX. Representative 2D tomogram slices of RDX- and TNT-based PBXs are shown in Figure 1b–c. Computer tomography with 1 μm pixel resolution did not show void spaces in X-PETN, or X-RDX suggesting that samples have, at most, sub-micron void spaces similar to prior work [4]. X-TNT and X-TATB tomograms showed larger crystals and occasional void space consistent with their lower observed density. No PDV signal was acquired off the PBX surface and thus to deal with the time zero problem in our log (time) plots, the time axis was arbitrarily set to define 10^{-9} s as the instant the emission came off the base line. Previous studies showed emission raise above the baseline several ns before shock arrival at the back window due to the finite optical depth of the sample [18].The absolute emission time relative to the flyer launch was shown to be consistent across all measured wells within the uncertainty in well thickness and shock transit time through the samples.

The 32-channel pyrometer has been described previously [4,1,19]. The light collected by the microscope objective was used to create a magnified image in the plane of a variable iris which was imaged by a 1:1 relay system to the variable slit of the spectrograph, which results in a rectangular imaged area which was 90×36 μm for X-PETN, X-RDX, and X-TNT and 90×54 μm for X-TATB. The enlarged area for X-TATB was necessary due to lower total signal. To enable radiometric measurements, the spectrometer was calibrated by imaging the exit port of an integrating sphere with a flat, spatially uniform, and NIST-traceable radiometrically-calibrated output (LabSphere Inc.). This calibration implicitly accounts for the varying observation area between experiments. Graybody methods for temperature fitting have been described previously [17,19].

Briefly, Plank's Law, Eq. (1), gives the spectral radiance L of a thermal body,

$$L(T,\lambda)d\lambda = \varepsilon \cdot \frac{2hc^2 d\lambda}{\lambda^5 \left[e^{\frac{hc}{kT\lambda}} - 1 \right]},\tag{1}$$

where ε is the graybody emissivity. To account for spatial inhomogeneity in emission, which cannot be corrected for in calibration, we modified Eq. (1) by defining the parameter $\Phi = \varepsilon^* V^*$, where Φ is the spatially-averaged emissivity measured by our spectrometer, ε is the graybody emissivity, and V^* the volume fraction of emitters. This can be used as a metric to qualitatively asses what portion of the sample is reacting. For example, if an increase in driven shock pressure increase the number density of reactive sites without changing the reactive site temperature, the observed emission will increase proportionally in intensity with no change to the spectral shape.

To acquire emission transients, the digitizer outputs were binned using a log(time) algorithm, where the data were averaged into 15 points per time decade. This greatly improved the signal-to-noise ratio in the later decades, be-cause each data point was the average of more acquisitions than the previous. Furthermore, at each flyer velocity we acquired typically 25 emission transients and averaged together their spectral radiance before making temperature and spatially emissivity fits. The high throughput of our impactor system makes it uniquely capable to perform signal-averaged measurements of impactor-driven experiments. The 95% confidence limit of the spectral radiance fits for temperature measurements was typically within 5%; however, due to the stochastic nature of reaction site generation and the large temperature dependence of radiance, $T^{>4}$ over this temperature and spectral range, which allows a small temperature band to represent a much larger spatially-averaged emissivity, the standard deviation of Φ was typically within 50% during the first decade and within 30% thereafter. This high order dependence of radiance on temperature is also the origin of the well-known bias in optical pyrometry to the hottest temperatures within an area. We examined the shots in each set to see if there were any outliers, which were discarded. No more than 2 outliers were found per speed, typically 0 or 1. We believe outliers occurred when the sample wells were not properly filled or reaction from a previous shot damaged either the target or flyer plate.

3 Results and Discussion

Averaged temperature histories for X-PETN are shown in Figure 2a. Error bars for temperature and Φ are given as the 95% confidence limit (1.96 standard deviations). They are consistent across all impact velocities, with relative values as discussed in the previous section. The temperature dynamics as a function of impact velocity appear to be bimodal, showing a low impact velocity regime (1.5–3.4 km s^{-1}) and a high impact velocity regime (3.6–4.5 km s^{-1}). Additional impact velocities have been collected, but are omitted for clarity. The omitted velocities are chosen such that no significant changes are seen between shown data sets. In the lower velocity regime, the temperature dynamics appear consistent with previously published results on PETN-based PBXs where single shots were shown rather than the dynamics shown here which were taken from the averaged spectral radiance of many shots [4]. The high impact velocity regime shows a greatly increased cooling rate at early times due to driving a shock near the von-Neumann spike pressure and generating an overdriven detonation condition which has recently been discussed [20].

The temperature dynamics for X-RDX are shown in Figure 2b. Contrary to the X-PETN, the temperature at lower impact velocities does not monotonically decrease. Rather the temperature increases until ~25 ns. As impact velocity and thus shock pressure increases, the magnitude of the temperature rise at ~25 ns decreases. At 3.5 km s^{-1} the temperature spike no longer increases above the initial hot spot temperature and begins cooling at an increased rate.
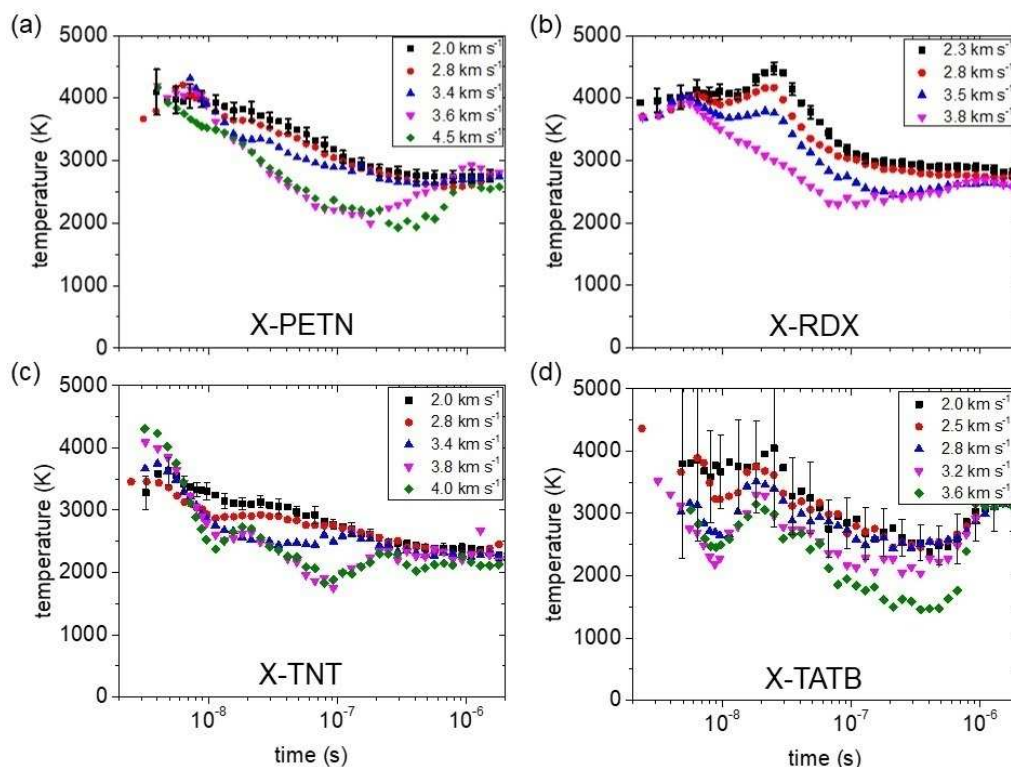
Figure 2. Temperature dynamics of (a) X-PETN, (b) X-RDX, (c) X-TNT, and (d) X-TATB at a range of impact velocities. Error bars are omitted from all but the slowest velocity for clarity. Typical relative error is ~5% for the first decade (i.e. until 10^{-8} s) and ~3% thereafter, with the exception of X-TATB. See text for details. Note the logarithmic time axis.

At an impact velocity of 3.8 km s^{-1} the temperature increase is completely gone and the temperature cools monotonically similarly to X-PETN. Similar to X-PETN, the temperature converges to 2800 K near 1 μs after impact.

Average temperature histories for X-TNT are shown in Figure 2c. At the lowest impact velocities (2.0–2.8 km s^{-1}) the hot spots cool at a consistent rate throughout the reaction, while at higher impact velocities there is a faster initial cooling into a plateau temperature which lasts for hundreds of nanoseconds at 3.4 km s^{-1} and 20 ns at higher pressures before additional cooling is observed. By 200 ns the temperatures converge to 2500 K, which is the lowest final temperature of any formulation studied here. Between 3.4 and 3.8 km s^{-1} the initial hot spot temperature increases by ~1000 K. Even though the initial temperature increases here, the temperature at t = 10 ns remains constant at ~2500 K indicating that the hot spot cooling rate has increased between these two speeds.

We recently showed that to accurately determine temperature in a TATB-based material, where spectra are not strictly thermal, the absorption of the material must be accounted for by either including a Gaussian term in the graybody fitting function or fitting the thermal spectrum using only the wavelengths between 650 nm and 800 nm [21]. Average temperature dynamics for X-TATB are shown in Figure 2d where the graybody fit was made using only

wavelength channels between 650 nm and 800 nm. The reduction in fitting channels causes a larger uncertainty. Due to this uncertainty X-TATB is shown for completeness, but will not be discussed in detail.

The first 100 ns of temperature dynamics, radiance, and spatially-averaged emissivity for all four PBX formulations at two impact velocities, 2.8 km s^{-1} and 4.0 km s^{-1} are shown in linear time in Figure 3. The initial hot spot temperature is seen to be 4000 K in both X-PETN and X-RDX, and the temperatures evolve similarly with the exception of the temperature spike in the RDX-based material. In X-TNT, the initial hot spot temperature is similar to that of X-PETN and X-RDX, but cools more quickly than either. After 10 ns, when the shock is unloading, the temperature difference between X-TNT and X-PETN and X-RDX has increased to 1000 K. Hot spots in X-TATB form at a modest 3000 K, the lowest temperature of any formulation studied here, and exhibit a temperature increase over the first 30 ns, similar to X-RDX. At the highest impact velocity the temperature dynamics of X-PETN and X-RDX have nearly completely converged. At this velocity, X-TNT is observed to have the same initial temperature as X-PETN and X-RDX; however, it quickly cools to much cooler than either. X-TNT appears to be the only formulation for which a significant change in initial temperature is observed. At this higher velocity X-TATB continues to exhibit relatively low temperature hot spots and their

W. P. Bassett, B. P. Johnson, D. D. Dlott
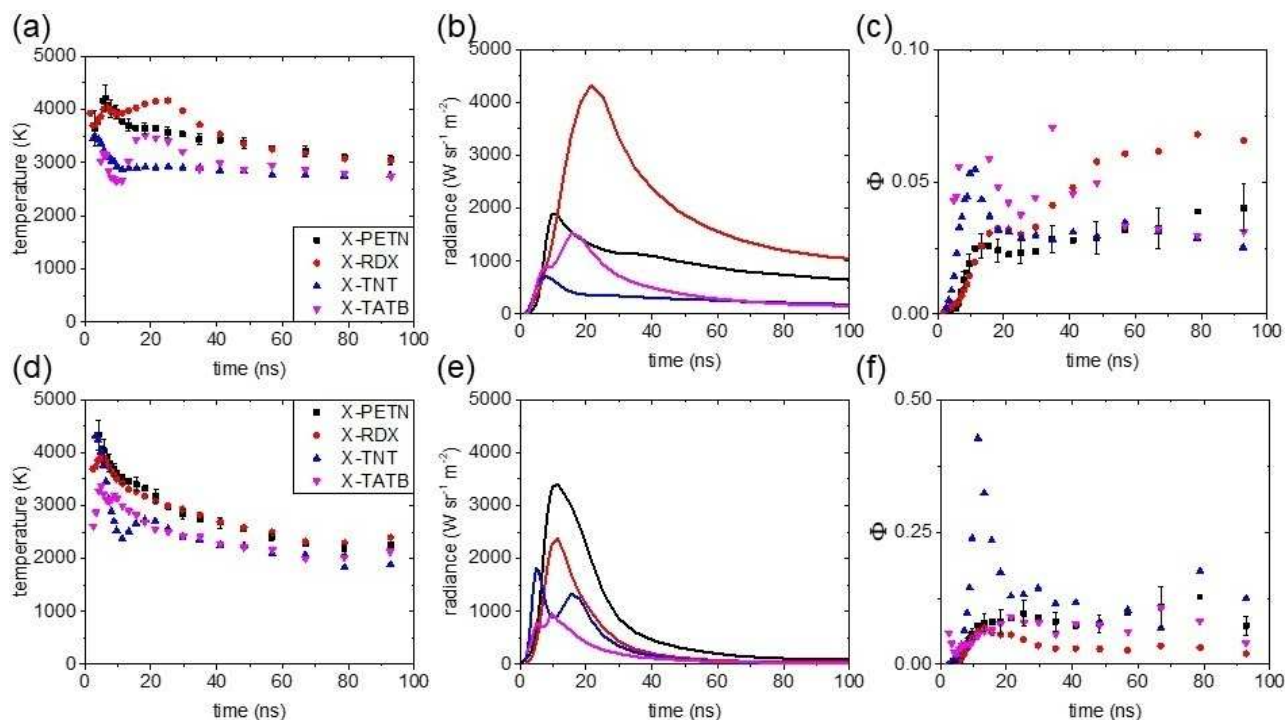
Figure 3. Averaged temperature dynamics (a,d), radiance (b,e), and spatially-averaged emissivity (c,f) for low velocity (a–c), and high velocity (d–f) impacts. The top row represents low velocity impacts, where the flyer plate impacted at 2.8 km s^{-1} in all cases. The bottom row represents high velocity impacts, where the flyer plate impacted at 4.0 km s^{-1} in all cases. Note the linear time axis and differing scales in Φ.

temperature increase is pushed earlier in time. The radiance during hot spot formation lasts much longer at low velocities, especially for X-RDX which is the only formulation where the radiance peak is out as late as 20 ns. At 2.8 km s^{-1} the radiance never falls to the noise floor of the instrument. At the higher impact velocities used here, all formulations yielded limited radiance after the initial ~40 ns. This fast cooling is likely due to rapid adiabatic expansion from a detonating charge, as recently seen in X-PETN [20].

Spectral radiance (i. e. the spectrally resolved emission) for a 2.8 km s^{-1} impact at various impact times is given in Figure 4 for all formulations. X-TATB shows strong deviations from graybody behavior [21]; however, the PETN, RDX, and TNT emission is well-fit by the graybody model. The relative temperatures are seen from the spectral shape with X-RDX being the hottest through this period and X-TNT being the coolest. The 10, 15, and 20 ns times chosen here represent the rising edge and peak of emission in X-RDX and the peak and falling edge in X-PETN and X-TNT. The spectral quality demonstrated is representative of all times and impact conditions studied here over the range from 1.5 to 4 km s^{-1} for these materials.
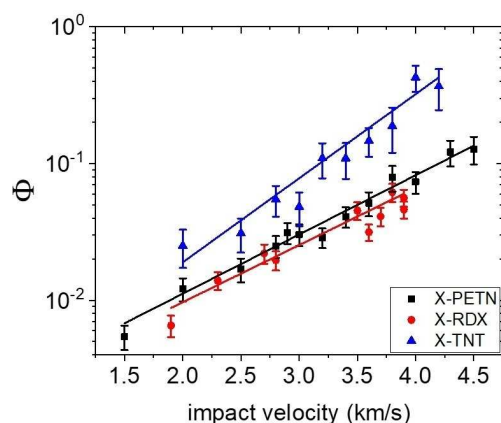
The spatially-averaged emissivity at t = 11 ns is shown in Figure 5 for PETN, RDX, and TNT-based formulations at impact velocities ranging from 1.5 km s^{-1} to 4.5 km s^{-1}. This time was chosen due to the peak in emissivity that is seen

in all formulations at all impact velocities except for X-RDX, where the peak occurs about 5 ns later at low velocities. Due to the increased uncertainty in X-TATB, it has been omitted. In all cases the Φ parameter increases with increasing impact velocity, indicating a larger volume of reaction sites. The formulations appear to follow an exponential growth (solid lines) in Φ and the exponential growth parameter of X-PETN, X-RDX, and X-TNT are 1.00 ± 0.04, 0.96 ± 0.08, and 1.42 ± 0.07 s km^{-1}, respectively. We recently described the emissivity dependence on impact velocity in X-PETN as quadratic, indicating a linear relationship between the energy barrier to collapse a hot spot-yielding pore and the input shock energy [20]. The alternate paradigm presented here, which is equally well-fit over the range of impact velocities for X-PETN and a better fit when including X-RDX and X-TNT, would suggest that the energy barrier is exponential in shock energy rather than linear. Additional experiments either to extend the impact velocity range or improve the measurement resolution are needed to determine the correct dependence. Theoretical models could similarly be used to elucidate the relationship between the barrier to hot spot formation and shock pressure/energy.

In ZND theory, the initial shock up to the von-Neumann spike is a purely compressional process in which no chemistry occurs [22]. Chemistry to convert starting material into products after the von-Neumann spike occurs in the so-
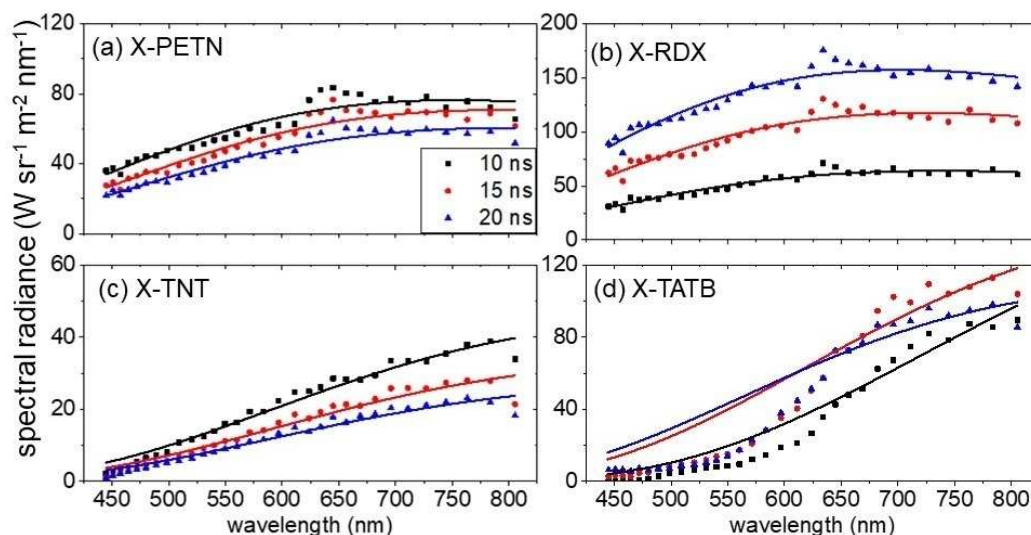
Figure 4. Spectral radiance for (a) X-PETN, (b) X-RDX, (c) X-TNT, and (d) X-TATB at the indicated times relative to observed emission. Solid symbols represent the measured data points. Solid lines represent the graybody model fit with all wavelengths for (a)–(c) and 650 nm– 800 nm channels in (d).

Figure 5. Shock strength dependence on spatially averaged emissivity at t = 11 ns for (a) X-PETN (black squares), (b) X-RDX (red circles), and (c) X-TNT (blue triangles). Solid lines represent exponential growth fit lines.

called reaction zone. Following the reaction zone, the products reach the CJ point, where chemical equilibrium is achieved and thus no chemical reaction occurs to liberate additional heat [22]. PETN is known to behave in a way that is consistent with pure CJ theory, not showing evidence of a reaction zone on the several ns time scale of previous experiments [15]. The lack of heating observed in the temperature evolution of PETN hot spots is consistent with the idea that PETN's energy is released within the time-resolution of the instrument (~2 ns) and so the only observed dynamics result from cooling mechanisms, while RDX generates heat for several dozen nanoseconds after impact which competes with heat loss to yield the observed temperature dynamics [14]. In this view, the temperature evolu-

tion of hot spots in RDX is a measure of the temperature inside the evolving reaction zone. This analysis does not indicate that all chemical reaction in the system is instantaneous in PETN and slower in RDX, but rather that the portion of the system which is visible to thermal emission (i.e. the hottest hot spots) is reacted in this time frame. Clearly additional chemical reaction occurs in the system as the hot spots interact with the bulk PBX; however, this reaction is not visible to our emission spectrometer due to the relatively low temperature compared to the hot spots.

Figure 2 clearly shows a marked difference in not only hot spot generation temperatures, but also the temperature evolution of these hot spots within different explosive materials. The hot spot chemistry behaves differently as a function of shock pressure for each material and cannot be described by a global shock-pressure dependent model. For instance, while the PETN and RDX-based materials have nearly identical temperature dynamics at high shock pressures, X-PETN has two distinct regimes while X-RDX undergoes a gradual shift from low shock pressure behavior to high shock pressure behavior. The temperature evolution of X-PETN is best modeled as pure cooling, while the RDX-based material requires heat generation to accurately characterize it. The existence of two distinct regimes in PETN may indicate that the hot spot chemistry of PETN is invariant until a sufficiently high pressure drives a mechanistic change in chemistry. In contrast, the heating observed in RDX undergoes a gradual change, indicating that the slower heat release may result from chemical reaction with a pressure dependence.

The fact that shock pressure has minimal effect on the initial hot spot temperature, while simultaneously exponentially increasing the spatially-averaged emissivity is

indicative that the reactive sites may not be interacting within the low shock pressure regime. If we assume that change in emissivity due to a change in the chemistry of the reactive sites with respect to shock strength is small compared to the change in reacting volume (i.e. $\Delta\varepsilon \ll \Delta V^*$, $\Delta\Phi = \Delta V^*$) then the increase in Φ can result from two sources, either an increase in number density of reactive sites, or an increase in volume of individual reactive sites at a near constant number density. An increasing number density of isolated reactive sites would increase the observed reacting volume fraction without causing changes in temperature dynamics, such as would be expected with a change in chemical environment when a reaction site is confined by shocked, unreacted material rather than shocked, reacting material.

The initial hot spot temperature is controlled by the fast, fundamental chemistry which occurs during shock compression and yields lower temperatures for the materials with a higher activation energy and less favorable reactions such as carbon formation [23]. As shown by the temperature jump to the initial hot spot temperature, the initial chemistry that yields hot spots occurs within the time-resolution of our instrument. The immediacy of the temperature jump is consistent with theoretical works where significant loss of EM and generation of reaction products occurs on the 100 ps time scale, thus the major reactions and liberation of energy occurs in this period [12]. The initial temperature is also known to be affected by changes in microstructure of a PBX [4]. For example, the initial hot spot temperature has been observed to vary among batches of X-PETN from 3700–4500 K while remaining consistent to within 300 K for a single batch. The change in hot spot temperature evolution without a change in initial temperature is interpreted as a change in the confining layer around the hot spot, which would result in altered reactivity once a given hot spot is created, without affecting the hot spot genesis temperature. X-TNT was the only formulation where a large change in initial temperature was correlated to increasing shock pressure, indicating that the initial chemistry which creates hot spots may be more shock pressure dependent than in PETN or RDX-based materials.

For TNT and TATB-based materials, a lesser amount of energy is released over longer time scales [24], failing to compete with the heat loss mechanisms as well as X-RDX which results in a lower overall temperature. This is consistent with known properties of both TNT and TATB, where ~80 ns are required to release the bulk of their energy [14]. The increased cooling rate seen in X-TNT could also be due to the higher thermal conductivity of solid carbon products such as graphitic sheets and amorphous carbon known to form from reaction of TNT [5,1,26]. While the Φ parameter is frequently used to infer a relative change in the number density of reaction sites [18], for carbon-rich, aromatic explosives such as TNT or TATB it is important to recall that it is also representative of the material emissivity. For HEs known to produce carbon-heavy soot [5,27], the high Φ

could be indicative of either an increased hot spot density due to the larger-scale microstructure or the production of high emissivity carbon materials [28]. These high-carbon products form to a lesser extent in RDX and almost not at all in PETN [25,27].

For all formulations studied here, hot spot temperature evolutions were found to be only mildly affected by shock strength for weak shocks. For flyer impacts between 1.5 and 2.8 km s^{-1} temperature dynamics remained relatively consistent, while the spatially-averaged emissivity exponentially decreased with decreasing impact velocity until no emission was discernible. Clearly at some lower boundary for shock pressure the hot spot genesis process must change; however in the range studied here the results are consistent with a modified interpretation of the classic hot spot model [23,29]. In our experiments individual charges are 42 µm thick and have a volume of ~50 µg, only 25 % of which is driven by our impactor. While this precludes us from making quantitative descriptions of threshold shock pressures for detonation, we do obtain information about sensitivity of our PBX formulations from the initial temperature and rate at which hot spot creation increases with shock pressure. In the hot spot view where a critical, spatially-constrained temperature must be reached [23], the likelihood of criticality is based on two things: the initial temperature at which hot spots are formed and the spatial proximity of individual hot spots to one another such that their coalescence will form a large enough thermalized volume of sufficient temperature. In this view, a lower number density of hotter spots will thermalize equivalently to a higher number density of lower temperature spots. If the initial hot spot temperature is material dependent, such as shown here, sensitivity should trend upwards with increasing initial temperature. This general trend is observed in our PBX base HEs, with RDX and PETN having the highest initial temperature and sensitivity followed by TNT and TATB respectively [30]. Sensitivity of HE is well-known to increase with pore size and surface area [10,11]. which we have observed as having a substantial effect in initial hot spot temperature due to shock-induced decomposition and subsequent product compression [4]. The X-TNT and X-TATB formulations were shown to have significantly larger pore sizes, which correspond to a higher hot spot density, but showed lower temperatures due to their slower chemistry even when a tabletop detonation was acheived.

4 Conclusion

Hot spot genesis temperatures and temperature evolutions for 4 formulations are presented. The formulations consist of either PETN, RDX, TNT, or TATB in a 80/20 wt.% mixture with a silicone elastomer binder. The temperature dynamics demonstrate a unique shock strength dependence for each base explosive with distinct behavioral regimes in PETN, a gradual cooling in RDX, and a uniquely increasing genesis

temperature in TNT. In strongly overdriven conditions the cooling rate of all explosives increases dramatically. TATB-based formulations were shown to have non-graybody emission which has recently been discussed in detail [21].

The number density of observed hot spots, as inferred from the spatially-averaged emissivity, increases exponentially with shock strength for PETN, RDX, and TNT-based formulations. Using the hot spot genesis temperature and rate of increase of hot spot number density, qualitative conclusions about sensitivity were drawn which are consistent with known properties of explosives. Hot spots appear to be largely non-interacting with chemistry that is dictated by the explosive reactant. PETN undergoes the quickest hot spot chemistry, faster than our instrument resolution (~ 2 ns) and consistent with pure CJ theory where chemical equilibrium occurs immediately behind the shock front and RDX is observed to release significant energy over 25 ns.

Acknowledgements

References

[1] D. E. Taylor, B. M. Rice, *Quantum-Informed Multiscale M&S for Energetic Materials, In Advances in Quantum Chemistry, Vol 69*, Sabin, J. R., Ed. Elsevier Academic Press Inc: San Diego, **2014**; *69*, 171–219.

[2] D. Stirpe, J. O. Johnson, J. Wackerle, Shock Initiation of XTX-8003 and Pressed PETN, *J. Appl. Phys.* **1970**, *41*, 3884–3893.

[3] C. A. Campos, *The Effects of Diameter and temperaure on XTX-8004 Detonation Velocity. Division, D., Ed.* Mason & Hanger-Silas Mason Co. - Pantex Plant: **1980**.

[4] W. P. Bassett, .B. P. Johnson, N. K. Neelakantan, K. S. Suslick, D. D. Dlott, Shock initiation of explosives: High temperature hot spots explained, *Appl. Phys. Lett.* **2017**, *111*, 061902.

[5] S. Bastea, Nanocarbon condensation in detonation, *Sci. Rep.* **2017**, *7*, 6.

[6] M. A. Wood, M. J. Cherukara, E. M. Kober, A. Strachan, Ultrafast Chemistry under Nonequilibrium Conditions and the Shock to Deflagration Transition at the Nanoscale, *J. Phys. Chem. C* **2015**, *119*, 22008–22015.

[7] T. R. Shan, R. R. Wixom, A. P. Thompson, Extended asymmetric hot region formation due to shockwave interactions following void collapse in shocked high explosive, *Phys. Rev. B.* **2016**, *94*.

[8] C. J. Wu, M. R. Manaa, L. E. Fried, *Tight binding molecular dynamic simulation of PETN decomposition at an extreme condition, In Materials Research at High Pressure*, Manaa, M. R.; Goncharov, A. F.; Hemley, R. J.; Bini, R., Eds. **2007**; *987*, 139–144.

[9] D. P. DeWitt, G. D. Nutter, *Theory & Practice of Radiation Thermometry.* John Wiley & Sons, Inc.: **1988**.

[10] A. Kapahi, H. S. Udaykumar, Dynamics of void collapse in shocked energetic materials: physics of void-void interactions, *Shock Waves* **2013**, *23*, 537–558.

[11] R. R. Wixom, A. S. Tappan, A. L. Brundage, R. Knepper, M. B. Ritchey, J. R. Michael, M. J. Rye, Characterization of pore morphology in molecular crystal explosives by focused ion-beam nanotomography, *J. Mater. Res.* **2011**, *25*, 1362–1370.

[12] M. R. Manaa, L. E. Fried, *The Reactivity of Energetic Materials Under High Pressure and Temperature, In Advances in Quantum Chemistry, Vol 69*, Sabin, J. R., Ed. **2014**; *69*, 221–252.

[13] E. L. Lee, C. M. Tarver, Phenomenological Model Of Shock Initiation In Hetergeneous Explosives, *Phys. Fluids* **1980**, *23*, 2362–2372.

[14] C. M. Tarver, Detonation Reaction Zones in Condensed Explosives, *AIP Conf. Proc.* **2006**, *845*, 1026–1029.

[15] G. L. Green, C. M. Tarver, D. J. Erskine, *Reaction Zone Structure In Supracompressed Detonating Explosives.* Office of the Chief of Naval Research OCNR: Portland, OR, **1989**; *113291*, 670–682.

[16] A. D. Curtis, A. A. Banishev, W. L. Shaw, D. D. Dlott, Laser-driven flyer plates for shock compression science: Launch and target impact probed by photon Doppler velocimetry, *Rev. Sci. Instrum.* **2014**, *85*, 043908.

[17] W. P. Bassett, D. D. Dlott, Multichannel emission spectrometer for high dynamic range optical pyrometry of shock-driven materials, *Rev. Sci. Instrum.* **2016**, *87*, 103107.

[18] W. P. Bassett, D. D. Dlott, High dynamic range emission measurements of shocked energetic materials: Octahydro-1,3,5,7-tetranitro-1,3,5,7-tetrazocine (HMX), *J. Appl. Phys.* **2016**, *119*, 11.

[19] W. P. Bassett, D. D. Dlott, Shock initiation of explosives: Temperature spikes and growth spurts, *Appl. Phys. Lett.* **2016**, *109*, 091903.

[20] W. P. Bassett, B. P. Johnson, L. Salvati III, D. D. Dlott, Hot-spot generation and growth in shocked plastic-bonded explosives studied by optical pyrometry, *J. Appl. Phys.* **2019**, *125*, 215904.

[21] W. P. Bassett, B. P. Johnson, D. D. Dlott, Dynamic absorption in optical pyrometry of hot spots in plastic-bonded triaminotrinitrobenzene, *Appl. Phys. Lett.* **2019**, *114*, 194101.

[22] S. A. Sheffield, D. D. Bloomquist, C. M. Tarver, Subnanosecond measurements of detonation fronts in solid high explosives, *J. Chem. Phys.* **1984**, *80*, 3831–3844.

[23] C. M. Tarver, S. K. Chidester, A. L. Nichols, Critical conditions for impact- and shock-induced hot spots in solid explosives, *J. Phys. Chem.* **1996**, *100*, 5794–5799.

[24] B. M. Dobratz, Lawrence Livermore National, L., *LLNL explosives handbook: properties of chemical explosives and explosive simulants.* Lawrence Livermore National Laboratory, University of California; Available from National Technical Information Service: Livermore, Calif. Springfield, Va., **1985**.

[25] J. W. Kury, R. D. Breithaupt, C. M. Tarver, Detonation waves in trinitrotoluene, *Shock Waves* **1999**, *9*, 227–237.

[26] G. Fugallo, A. Cepellotti, L. Paulatto, M. Lazzeri, N. Marzari, F. Mauri, Thermal Conductivity of Graphene and Graphite: Collective Excitations and Mean Free Paths, *Nano Lett.* **2014**, *14*, 6109–6114.

[27] T. M. Willey, M. Bagge-Hansen, L. Lauderbach, R. Hodgin, D. Hansen, C. May, T. v. Buuren, D. M. Dattelbaum, R. L. Gustavsen, E. B. Watkins, M. A. Firestone, B. J. Jensen, T. Graber, S. Bastea, L. Fried, Measurement of carbon condensates using small-angle x-ray scattering during detonation of high explosives, *AIP Conf. Proc.* **2017**, *1793*, 030012.

[28] *CRC Handbook of Chemistry and Physics.* 97th ed.; CRC Press/ Taylor & Francis: Boca Raton, Fl, **2017**.

[29] J. E. Field, Hot-Spot Ignition Mechanisms For Explosives, *Acc. Chem. Res.* **1992**, *25*, 489–496.

[30] A. Macek, Sensitivity of Explosives, *Chem. Rev.* **1962**, *62*, 41–63.